

AEROSOLS

EVAN DAVID WELLMMEYER

M.Sc. Atmospheric Science and Technology

Course in Environmental Meteorology

Dr. Giovanni Pitari

Università Degli Studi Dell'Aquila, L'Aquila

Sapienza Università Di Roma, Rome

Fall 2021

1 Introduction

The study of particulate matter (PM) in the atmosphere is of growing concern due to their relation to human health, climate change and air pollution in general [1]. Moreover, aerosols have a direct radiative forcing effect since they scatter and absorb solar and infrared radiation in the atmosphere [2]. PM exists in a spectrum of forms and originating from many sources. PM detected in a site is a mixture of natural and anthropogenic primary and secondary aerosols which could be locally emitted or transported from other sites [1]. PM mass concentrations at the ground surface are a good indicator of in-situ pollution and its evolution during daytime only when local sources of aerosol dominate the aerosol mass balance [1]. The primary aerosols are generally those emitted into the atmosphere through mechanical processes such as Saharan dust and sea salt, where as secondary aerosols are those produced through chemicals processes of gases already present or emitted into the atmosphere such as sulfates and secondary organics [2].

1.0.1 Dust

One major contributor to aerosol loading and optical thickness, especially in sub-tropical and tropical regions, is soil dust from deserts and dry lake beds as well as areas where vegetation has been reduced or soil surfaces have been disturbed—such as those through agricultural processes [2]. One estimation from 1995 puts up to 50% of the atmospheric dust load originating from disturbed soil surfaces—a prospect suggesting anthropogenic origin [3]; however, this estimate is suggested to be considered highly uncertain [2]. Primary aerosol distributions have also been correlated to climatic oscillations—such as Saharan dust transport to the Caribbean increasing during El Niño years [4], or correlations between dust export to the Mediterranean and the North Atlantic Oscillation [5][2]. Soil dust is mainly coarse mode particles with a diameter ranging 1-10 μm , therefore contributing a significant optical depth in the planetary infrared spectrum [6].

1.0.2 Sea Salt

The generation of sea salt aerosols in marine regions is found to have a strong dependence on wind speed [2]. Sea salt aerosols may be the dominant contributor to both light scattering and cloud nucleation in regions of marine atmosphere with high wind speeds and relatively weak sources for other aerosols [7][8][9][2]. Sea salt aerosols can exhibit a wide range of diameters—from 0.05 – 10 μm in diameter, leading to diverse range of atmospheric lifetimes [2].

Anthropogenic primary aerosols, or Industrial dust, sources include transportation, coal combustion, cement manufacturing, metallurgy and waste incineration, which are responsible for the impact of anthropogenic aerosols on environmental quality [2]. Most industrial dust is present in a size above 1 μm , making it relatively optically inactive and therefore not of climatic importance. However, the emission of industrial dust has been reduced significantly due to close monitoring and regulation.

1.0.3 Carbonaceous Aerosols

Carbonaceous aerosols, including organic and black carbon, make up a significant—yet highly variable—fraction of atmospheric aerosols. Organic carbon makes up the largest percentage of the aerosols produced from biomass burning [10], and make up a large percentage of upper-tropospheric aerosols as well [11][2]. The presence of polar

functional groups makes many of the organic aerosols water soluble, leading cloud droplet nucleation. The main sources for carbonaceous aerosols are biomass and fossil fuel burning, and the atmospheric oxidation of biogenic and anthropogenic VOCs [2]. Atmospheric oxidation of biogenic hydrocarbons yields compounds of low volatility that readily form aerosols.

1.0.4 Nitrate

Nitrate aerosols are correlated to the relative abundances of ammonium and sulphate. If ammonia is available in excess of the amount required to neutralise sulphuric acid, nitrate can form small, radiatively efficient aerosols [2]. In the presence of accumulation-mode sulphuric acid containing aerosols, nitric acid deposits on larger, alkaline mineral or salt particles [12].

1.0.5 Sulphate and Volcanic Sources

Sulphate aerosols are produced by chemical reactions in the atmosphere by gaseous precursors. The two main sulphate precursors are SO_2 from anthropogenic sources and volcanoes, and Dimethyl sulfide (DMS) from biogenic sources [2]. Two components of volcanic emissions are of most significance for aerosols: primary dust and gaseous sulphur. Sulphur emissions occur mainly in the form of SO_2 , even though other sulphur species may be present in the volcanic plume, predominantly SO_4^{2-} aerosols and H_2S [2][13]. Volcanic sources are important to the sulphate aerosol burden in the upper troposphere, where they can contribute to the formation of ice particles and thus represent a potential for a large indirect radiative effect [14].

1.0.6 Relevant Aerosols in Southern Europe

Figure 1 shows the average annual source strength for Earth, where the European region shows a presence of natural and anthropogenic sulfate, organic matter, black carbon, sea salt and dust. A particular source of PM in southern Europe is soil dust from the Sahara desert in the northern part of Africa, which is raised by turbulent and convective winds and injected into the mid-troposphere [1]. Dust uplift above the boundary layer may then be followed by large scale horizontal transport, taking place in the free troposphere toward the Mediterranean basin and central Europe, sometimes reaching Northern Europe and the Arctic region [15][6] where it is deposited by wet and dry processes [1]. Outbreaks of desert dust from the Sahara combined with with local vertical mixing contributes to daily increases in PM_{10} observations [6]. Atlantic low-pressure troughs extending far south to the west coast of Morocco coupled to a high-pressure ridge over Northern Africa and the Mediterranean creates the most favorable meteorological conditions for strong outbreaks of Saharan dust in Europe, where a strong convergence can induce northerly flow lasting several days [15][6]. Another significant source of PM is emissions due to combustion processes and natural or deliberate fires of grassland and forests, which have an impact on the atmospheric composition and aerosol load both locally and globally [1].

1.0.7 Uncertainties

For primary aerosols, the largest uncertainties usually come from the extrapolation of experimentally determined source strengths to other regions and seasons. An example of this in southern Europe is the Sahara as a source for dust aerosols. Uncertainties in secondary aerosol species lie both in the sources of precursor gases as well as atmospheric processes converting some of these gases to aerosols [2].

1.0.8 PM classification

The classification of PM by size is an important part of determining the origin and behavior of aerosols present in the atmosphere, which can in turn help determine their contribution to radiative forcing as well as their atmospheric lifetime. The size classification of PM can be divided in three modes: the nucleation mode, pertaining to particles with a diameter from 1-100 nm; the accumulation mode for particles of size ranging 100 nm to 1 μm ; and the coarse mode for particles with a diameter greater than 1 μm . The accumulation mode is most relevant to radiative forcing as they determine the maximum extinction of incident solar radiation.

In this paper, PM modes are organized as follows: PM_1 refers to the summation of particle mass density up to 1 μm ; PM_{25} is the summation up to 2.5 μm ; PM_{10} is the summation to 10 μm ; and $\text{PM}_{\text{coarse}}$ is $\text{PM}_{10} - \text{PM}_1$.

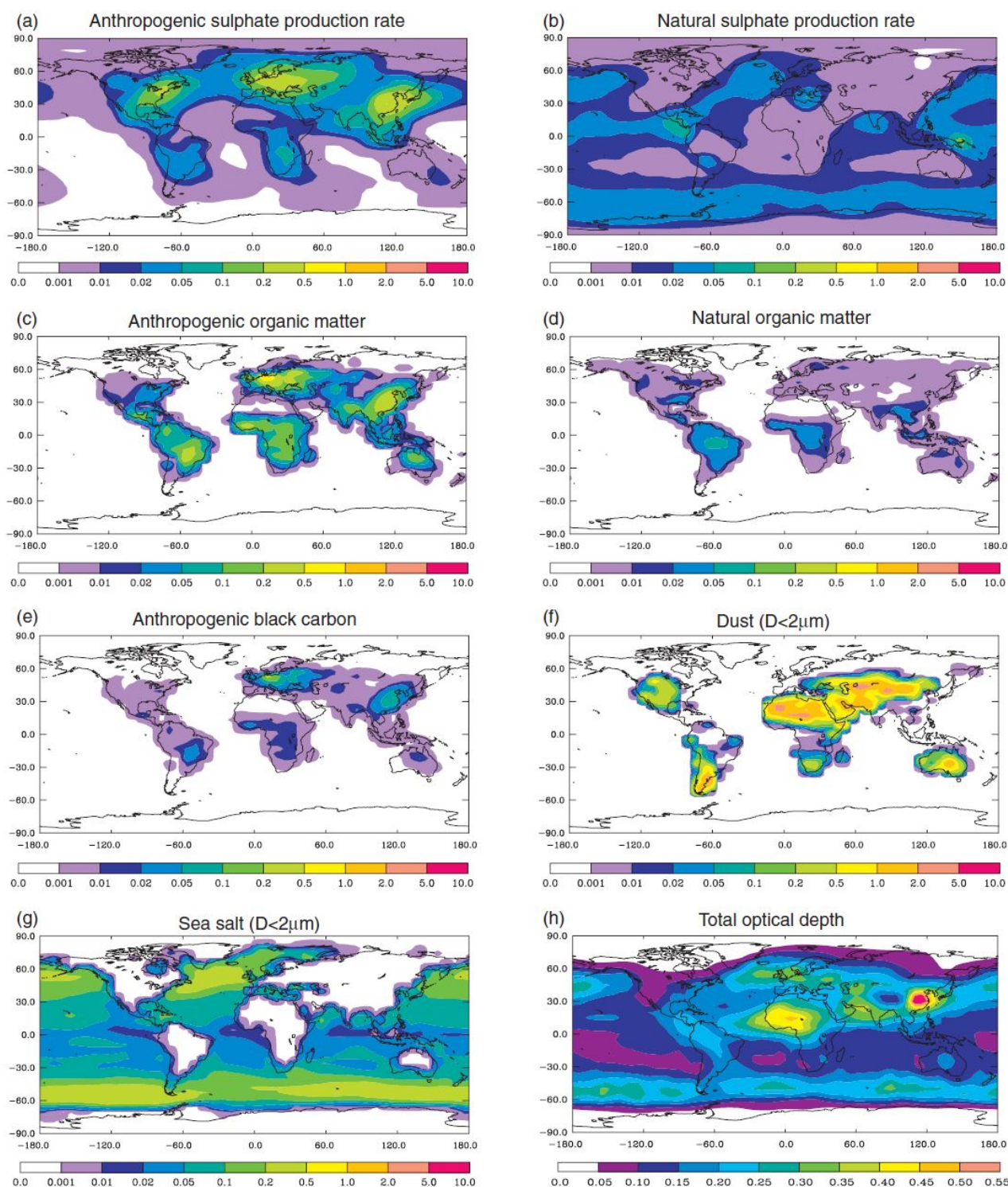


Figure 1: Annual average source strength in $\text{kg km}^{-2} \text{hr}^{-1}$ for multiple aerosol types, as well as total aerosol optical depth. Adapted from [2]

2 Data Collection

Aerosol and NO_x data were collected in the town of L'Aquila, located in central Italy. The continuous aerosol measurements were made via a multi-channel aerosol laser spectrometer. Aerosol particles can be counted in terms of total number of particles or in terms of total mass density. The multi-channel function allowed parallel storage of different aerosol concentrations. The specifications for measurements by each channel are recorded in Table 1.

Channel #	1	2	3	4	5	6	7	8	9	10	11	12	13	14
Diameter (μm)	0.23	0.30	0.40	0.50	0.65	0.80	0.90	1.0	2.0	3.0	4.0	5.0	7.5	10.0

Table 1: Differential accumulation channels of the aerosol laser spectrometer.

The resulting PM modes are obtained from the respective channels as follows: PM₁ is obtained as ch1 - ch8; PM₁₀ is ch1 - ch14; and PM_{coarse} is ch8, as seen in Table 2.

PM ₁	ch1 - ch8
PM ₁₀	ch1 - ch14
PM _{coarse}	ch8

Table 2: Calculation of PM modes from laser spectrometer channels.

2.1 Log-normal fit

When considering integrated aerosol mass of different modes, the aerosol mass in the boundary layer is almost evenly distributed in the fine mode and in the coarse mode, even though the number of particles in the coarse mode is an order of magnitude smaller than the number of particles in the fine mode. If we assume the particles are distributed according to the normalized Gaussian probability density function:

$$f(x) = \frac{1}{\sqrt{2\pi}\sigma} \exp\left\{-\frac{(x-x_0)^2}{2\sigma^2}\right\}$$

where $x_0 = E[x]$ is the expected value of x where $f(x)$ has its maximum and σ is the standard deviation defined as $\sigma^2 = E[(x-x_0)^2]$. The probability of finding an x value in a given finite interval $[x_1, x_2]$ is given by

$$F(x) = \int_{x_1}^{x_2} f(x) dx$$

Moving from the probability density function to the population density function, we have:

$$\begin{cases} x \rightarrow r : & \text{particle radius} \Rightarrow E[r] = r_0 ; E[(r-r_0)^2] = \sigma_r^2 \\ f(x) \rightarrow n(r) : & \text{number density function} \\ F(x) \rightarrow N(r) : & \text{number of particles in the integrated interval of } r \end{cases}$$

The normalized population density function is now

$$n(r) = \frac{1}{\sqrt{2\pi}\sigma_r} \exp\left\{-\frac{(r-r_0)^2}{2\sigma_r^2}\right\} = \frac{dN(r)}{dr}$$

In order to obtain the log-normal distribution we must multiply both members by r

$$r \cdot n(r) = r \cdot \frac{dN(r)}{dr} = \frac{dN(r)}{\frac{1}{r} \cdot dr} = \frac{dN(r)}{d \log(r)}$$

Moving from $r \rightarrow \log(r)$ the parameters of the distribution evolve as

$$E[\log(r)] = \log(r_0)$$

$$E[(\log(r) - \log(r_0))^2] = \log^2(\sigma_r)$$

$$N_0 = \int_{-\infty}^{+\infty} r \cdot n(r) d(\log(r)) = \int_{-\infty}^{+\infty} r \cdot n(r) \frac{1}{r} dr = \int_{-\infty}^{+\infty} n(r) dr$$

where N_0 is the normalization factor representing the total population of particles in the domain. The resulting log-normal population density function is:

$$r \cdot n(r) = \frac{N_0}{\sqrt{2\pi} \log(\sigma_r)} \exp\left\{-\frac{[\log(r) - \log(r_0)]^2}{2 \log^2(\sigma_r)}\right\}$$

Now we can see how it is possible to apply a parabolic fit the distribution. Applying the log function to both members:

$$\begin{aligned}
 \log(r \cdot n(r)) &= \log\left(\frac{N_0}{\sqrt{2\pi} \log(\sigma_r)} \exp\left\{-\frac{[\log(r) - \log(r_0)]^2}{2 \log^2(\sigma_r)}\right\}\right) \\
 &= \log\left(\frac{N_0}{\sqrt{2\pi} \log(\sigma_r)}\right) + \log\left(\exp\left\{-\frac{[\log(r) - \log(r_0)]^2}{2 \log^2(\sigma_r)}\right\}\right) \\
 &= \log\left(\frac{N_0}{\sqrt{2\pi} \log(\sigma_r)}\right) - \frac{[\log(r) - \log(r_0)]^2}{2 \log^2(\sigma_r)} \\
 &= \log\left(\frac{N_0}{\sqrt{2\pi} \log(\sigma_r)}\right) - \frac{\log^2(r) - 2 \log(r) \log(r_0) + \log^2(r_0)}{2 \log^2(\sigma_r)} \\
 \log(r \cdot n(r)) &= -\frac{\log^2(r)}{2 \log^2(\sigma_r)} + \frac{\log(r) \log(r_0)}{\log^2(\sigma_r)} - \frac{\log^2(r_0)}{2 \log^2(\sigma_r)} + \log\left(\frac{N_0}{\sqrt{2\pi} \log(\sigma_r)}\right)
 \end{aligned}$$

if we parameterize the terms as follows

$$\begin{cases}
 x = \log(r) \\
 y = \log(r \cdot n(r)) \\
 a = -\frac{1}{2 \log^2(\sigma_r)} \\
 b = \frac{\log(r_0)}{\log^2(\sigma_r)} \\
 c = -\frac{\log^2(r_0)}{2 \log^2(\sigma_r)} + \log\left(\frac{N_0}{\sqrt{2\pi} \log(\sigma_r)}\right)
 \end{cases}$$

the result is of the form

$$y = ax^2 + bx + c$$

From a it is possible to obtain the standard deviation

$$2 \log^2(\sigma_r) = -\frac{1}{a} \longrightarrow \log(\sigma_r) = \sqrt{-\frac{1}{2a}} \longrightarrow \sigma_r = \exp\left\{\frac{1}{\sqrt{-2a}}\right\}$$

From b it is possible to obtain the expected value

$$\log(r_0) = b \log^2(\sigma_r) \longrightarrow r_0 = \exp\{b \log^2(\sigma_r)\} \longrightarrow r_0 = \exp\left\{-\frac{b}{2a}\right\}$$

From a it is possible to obtain the normalization factor

$$\begin{aligned}
 \log\left(\frac{N_0}{\sqrt{2\pi} \log(\sigma_r)}\right) &= c + \frac{\log^2(r_0)}{2 \log^2(\sigma_r)} \longrightarrow \frac{N_0}{\sqrt{2\pi} \log(\sigma_r)} = \exp\left\{c + \frac{\log^2(r_0)}{2 \log^2(\sigma_r)}\right\} \\
 \longrightarrow N_0 &= \sqrt{2\pi} \log(\sigma_r) \exp\left\{c + \frac{\log^2(r_0)}{2 \log^2(\sigma_r)}\right\} = \sqrt{2\pi} \cdot \sqrt{-\frac{1}{2a}} \cdot \exp\left\{c + \frac{\left(-\frac{b}{2a}\right)^2}{-\frac{1}{2a}}\right\} \\
 N_0 &= \sqrt{\frac{\pi}{-a}} \cdot \exp\left\{c - \frac{b^2}{2a}\right\}
 \end{aligned}$$

Using measurement data $\{x_i, y_i\}$ it is possible to apply a parabolic fit to obtain the parameters a, b, c

3 Results and Discussion

A first step in considering the behavior of PM in the boundary layer is to analyze the concentration in the form of the diurnal cycle. Figure 2 shows the averaged diurnal cycle for NO_x and PM₁₀ over nine months from November 2006 to August 2007. The comparison between diurnal cycles of NO_x and PM₁₀ is useful since we have already considered the various factors shaping the diurnal cycle of NO_x.

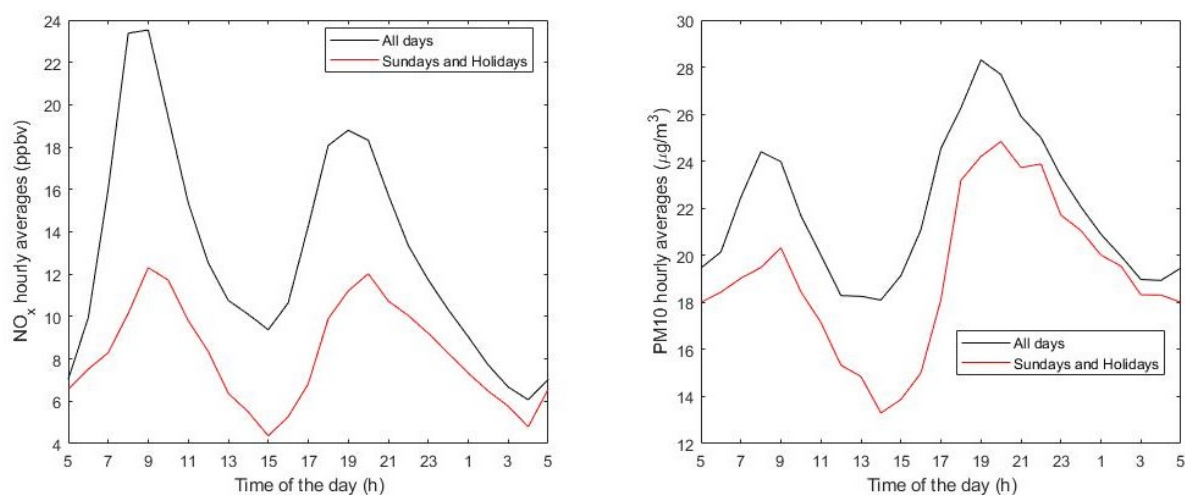


Figure 2: Diurnal cycles from 5 to 5 for hourly averages of NO_x and PM₁₀ between November 2006 and August 2007.

The similarities between the two diurnal cycles in Figure 2 suggests that secondary anthropogenic aerosols dominate in daytime hours, that the mechanical and chemical factors driving the NO_x diurnal cycle contribute similarly the precursors for production of PM₁₀. This is not always the case, such as in events of long range desert dust (PM₁₀) transport as seen on June 20-21 and June 25 in Figure 6.

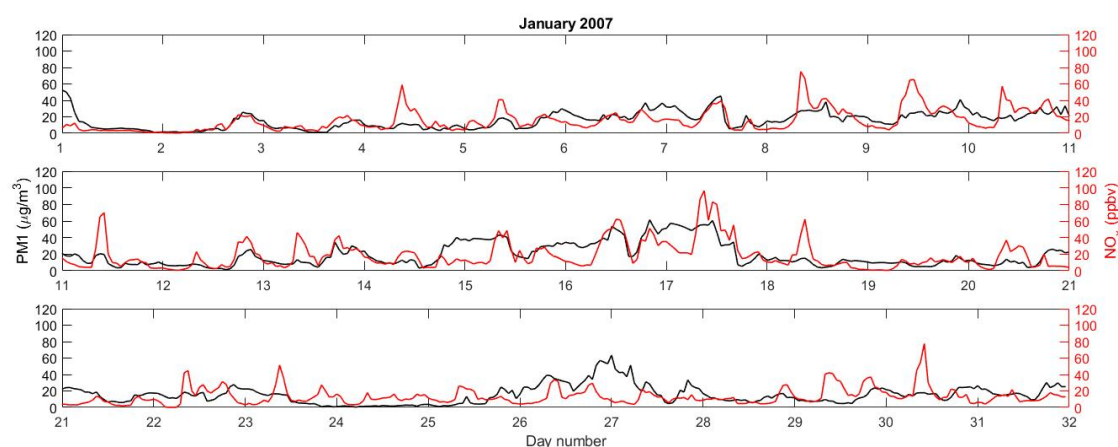


Figure 3: Time series for PM₁ and NO_x in January 2007.

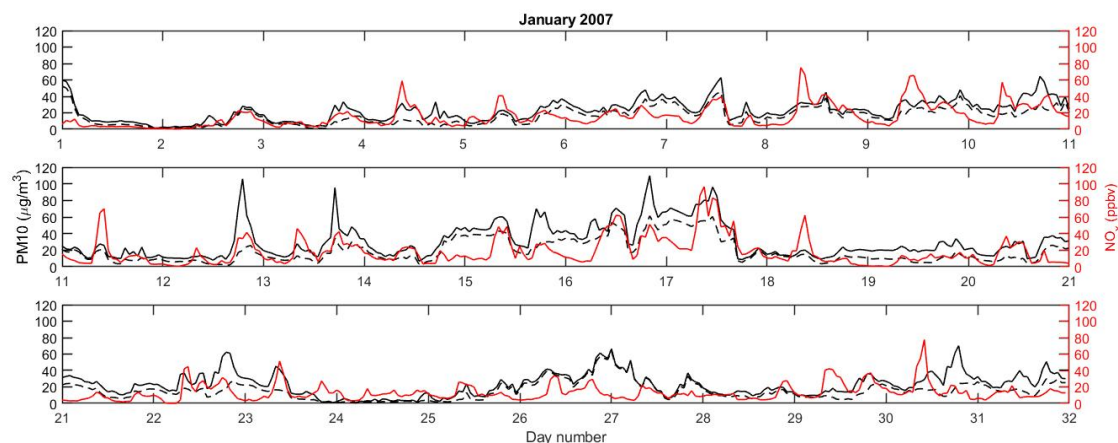
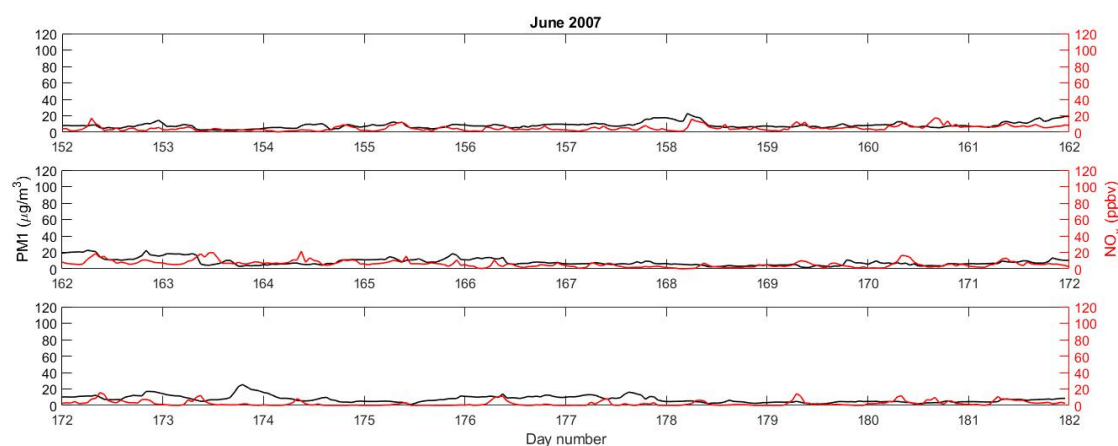
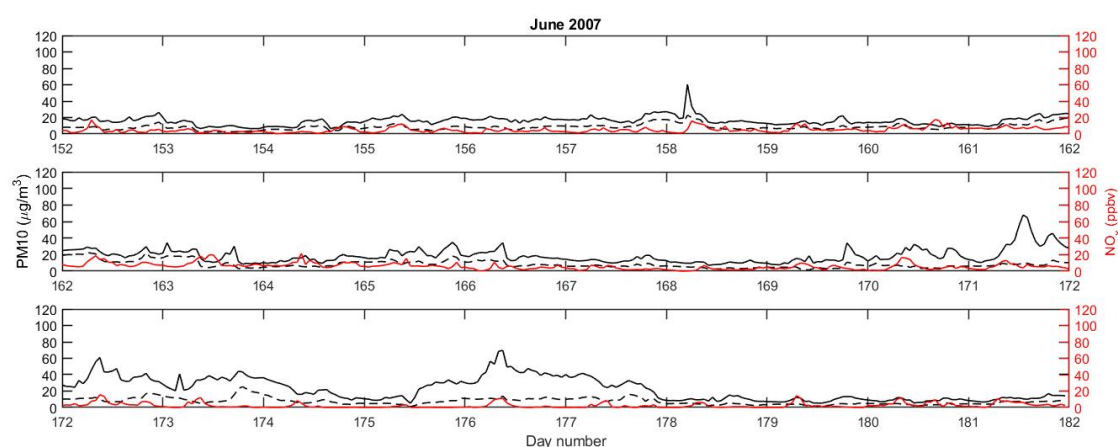


Figure 4: Time series for PM₁₀ and NO_x in January 2007.

Figure 5: Time series for PM₁ and NO_x in June 2007.Figure 6: Time series for PM₁₀ and NO_x in June 2007.

Comparing the time series of PM and NO_x from January (Figure 3-4) with the time series from June (Figure 5-6), there is a large difference in the relative abundances of both NO_x and PM between the winter and summer month. The general decrease in aerosol concentrations towards the summer season is caused by increasing mixing efficiency due to a convectively more unstable boundary layer [1].

Tables 3-5 show the correlations of the respective PM modes with rainfall, wind and NO_x for daytime hours, nighttime hours and total. There is little noteworthy about the differences in correlations between respective elements and the various PM modes; however, a significant generality can be made across all PM modes through the change of seasons such that the correlations decrease dramatically from winter into the summer months. A worthy note concerning tables 3-5

Month	Year	Rainfall	Wind	NO _x	NO _x day	NO _x night
December	2006	-0.6645	-0.4402	0.5273	0.5726	0.6293
January	2007	-0.4704	-0.4926	0.4613	0.6782	0.4231
February	2007	-0.4146	-0.3855	0.1568	0.2779	0.2596
March	2007	-0.4056	-0.3765	0.3183	0.4439	0.2780
April	2007	0.0996	-0.4196	0.1305	0.2670	0.1476
May	2007	0.1249	-0.3214	0.0114	0.1060	0.3350
June	2007	0.0397	-0.1432	0.1964	0.2429	0.4040

Table 3: Correlations with PM₁.

Month	Year	Rainfall	Wind	NOx	NOx day	NOx night
December	2006	-0.6800	-0.4455	0.6151	0.5940	0.7812
January	2007	-0.5048	-0.4464	0.5508	0.6972	0.5898
February	2007	-0.6079	-0.3330	0.2862	0.3954	0.4148
March	2007	-0.3265	-0.3234	0.3914	0.4734	0.4026
April	2007	0.1788	-0.3579	0.2155	0.3153	0.3319
May	2007	0.0480	-0.2196	0.0314	0.0545	0.3022
June	2007	0.0826	0.0866	0.0711	0.0600	0.3628

Table 4: Correlations with PM10.

Month	Year	Rainfall	Wind	NOx	NOx day	NOx night
December	2006	-0.6523	-0.2487	0.5552	0.3571	0.7913
January	2007	-0.2983	-0.1547	0.4140	0.4462	0.5135
February	2007	-0.4112	-0.0527	0.3052	0.3517	0.3809
March	2007	-0.1842	-0.0697	0.3864	0.3491	0.4374
April	2007	0.2071	-0.0049	0.2544	0.1923	0.4121
May	2007	-0.0137	0.0100	0.0579	0.0231	0.1080
June	2007	0.1117	0.2152	-0.0120	-0.0412	0.1001

Table 5: Correlations with PMcoarse.

is the negative correlations with wind and rain, signifying dispersion of aerosols by wind and wet deposition of PM by rain. Another note concerning NOx is that there is a higher correlation between all modes of PM and NOx during nighttime hours in comparison to daytime hours. The first reason for this discrepancy is the stability present in the atmosphere during nighttime, and the instability introduced by the sun during daytime hours; the second reason is that there is a massive reduction in anthropogenic precursors creating secondary aerosols in the nighttime—similar to those precursors contributing to NOx cycles that are more or less inert at nighttime. The collective correlations between the three PM modes are represented as a time series in Figure 7, where there is a clear convergence towards zero correlation in the summer months across all PM modes. It is an important to note that all modes here show the same behavior, despite an order of magnitude in size range. One small exception to this is the correlation between PMcoarse and wind, which is very low even in winter months.

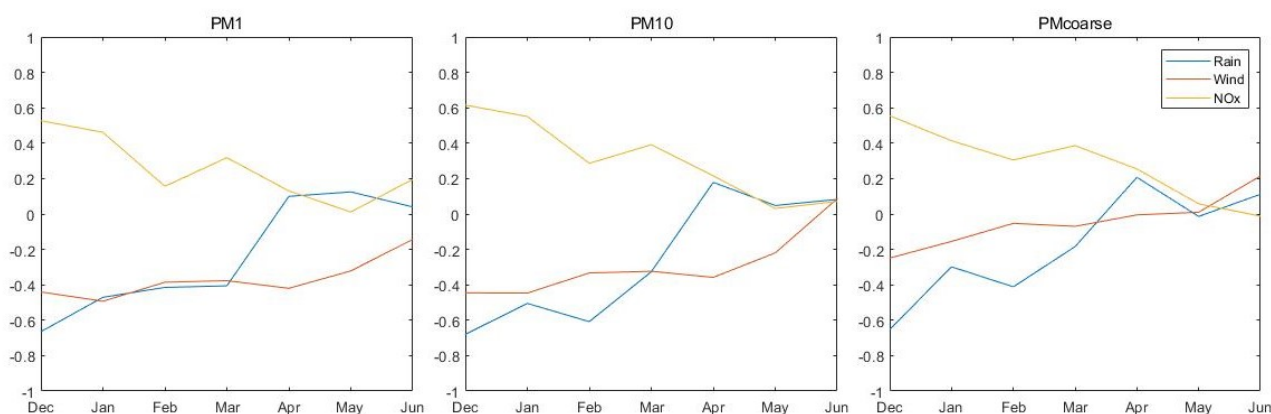


Figure 7: Plot of correlations for respective PM modes with rain, wind and NOx for months December - June.

Results from the application of the parabolic fit from the log-normal theory discussed earlier are present in the tables of Figures 8-10, where data present for the same months of different years have been averaged together. The first mode considers particles of radius less than $1\mu\text{m}$ and the second mode considers particles of radius greater than $1\mu\text{m}$. N01 and N02 in the first column represent the normalization factors for population density with $r_{.01N}$ and $r_{.02N}$ as the expectation values for the particle radius; M01 and M02 are the normalization factors for mass density with $r_{.01M}$ and $r_{.02M}$ as the expectations values, and Sigma1 and Sigma2 as the variance—all for the first and second modes, respectively. Table 8 shows a dominance of the first mode in winter months, with a small flip to dominance of the second mode in summer months. Expectation values and variance for the two modes are relatively consistent throughout the year.

Month	N01	r_01(N)	N02	r_02(N)	M01	r_01(M)	M02	r_02(M)	Sigma1	Sigma2
Jan	2561.8	0.071	0.72	0.766	21.35	0.169	9.01	2.07	1.71	1.78
Feb	1882.5	0.071	0.60	0.799	16.13	0.173	7.95	2.06	1.73	1.75
Mar	1652.2	0.069	0.97	0.537	14.54	0.183	6.21	1.82	1.77	1.89
Apr	2503.8	0.071	0.58	0.676	19.10	0.159	5.73	2.00	1.68	1.82
May	1192.2	0.064	1.71	0.541	10.70	0.197	11.28	1.91	1.84	1.91
Jun	1172.3	0.066	1.03	0.706	10.63	0.194	11.71	2.10	1.82	1.83
Jul	1527.8	0.065	1.44	0.548	12.14	0.181	11.11	2.17	1.79	1.97
Aug	1115.1	0.064	1.67	0.488	8.90	0.183	9.76	2.02	1.81	2.03
Sep	1199.3	0.062	2.29	0.638	11.62	0.214	19.49	1.92	1.90	1.83
Oct	2273.5	0.066	3.82	0.454	22.31	0.201	14.76	1.59	1.84	1.91
Nov	3934.9	0.073	0.85	0.841	33.96	0.169	12.24	2.06	1.70	1.73
Dec	4273.2	0.073	0.85	0.806	35.86	0.166	11.29	2.05	1.69	1.74

Figure 8: Normalization factors, expectation values and variance for the first and second mode of both population and mass density. Months with data from multiple years have been averaged.

The table of Figure 9 shows the correlations between the parabolic fit of the first and second modes with the measured values for both population density and mass density. The X-Y domain considers the log-normal distribution $dN/d\log r$, and the normal domain considers the normalized probability density function dN/dr . The correlations in the table show the fit is very accurate in representing both population density and mass density in both modes; moreover, the parabolic fit of the 2nd mode in the XY domain is particularly accurate.

Month	N(r) xy 1st	N(r) xy 2nd	N(r) norm 1st	N(r) norm 2nd	M(r) xy 1st	M(r) xy 2nd	M(r) norm 1st	M(r) norm 2nd
Jan	0.982	0.999	0.957	0.998	0.928	0.989	0.940	0.955
Feb	0.981	0.998	0.958	0.998	0.927	0.987	0.938	0.950
Mar	0.976	0.996	0.956	0.994	0.915	0.984	0.916	0.934
Apr	0.982	0.999	0.954	0.993	0.922	0.989	0.945	0.941
May	0.956	0.998	0.947	0.979	0.865	0.978	0.868	0.913
Jun	0.962	0.998	0.951	0.993	0.880	0.982	0.884	0.931
Jul	0.963	0.998	0.947	0.987	0.846	0.970	0.892	0.926
Aug	0.959	0.998	0.945	0.987	0.847	0.970	0.886	0.912
Sep	0.947	0.998	0.942	0.983	0.861	0.984	0.817	0.927
Oct	0.965	0.997	0.953	0.980	0.903	0.981	0.874	0.904
Nov	0.986	0.999	0.957	0.998	0.945	0.993	0.949	0.967
Dec	0.986	0.999	0.956	0.998	0.945	0.993	0.950	0.964

Figure 9: Correlations between the parabolic fit of the 1st and 2nd mode and the measured values for X-Y domain and the normal domain.

The table of Figure 10 total mass calculations from three different methods: Column 1 shows the total mass calculated from the parameters of the parabolic fit; column 2 shows the total mass calculated from the integral of the fit; and column 3 shows the sum of the differential mass of each mode. The values of each method are very similar, attributing to the reliability of the log-normal theory applied to atmospheric PM.

Month	Tot. Mass Param.	Tot. Mass Integ.	Sum diff. mass
Jan	30.36	29.42	31.28
Feb	24.07	23.28	24.57
Mar	20.75	19.60	21.00
Apr	24.83	24.19	26.52
May	21.97	20.30	22.07
Jun	22.34	21.10	22.31
Jul	23.25	21.82	23.83
Aug	18.66	17.46	18.99
Sep	31.12	28.72	30.69
Oct	37.07	33.48	36.50
Nov	45.94	44.74	47.07
Dec	47.17	45.97	48.72

Figure 10: Total mass calculated from the parameters of the fit, total mass by integrating the fit and sum of the differential mass for the two modes.

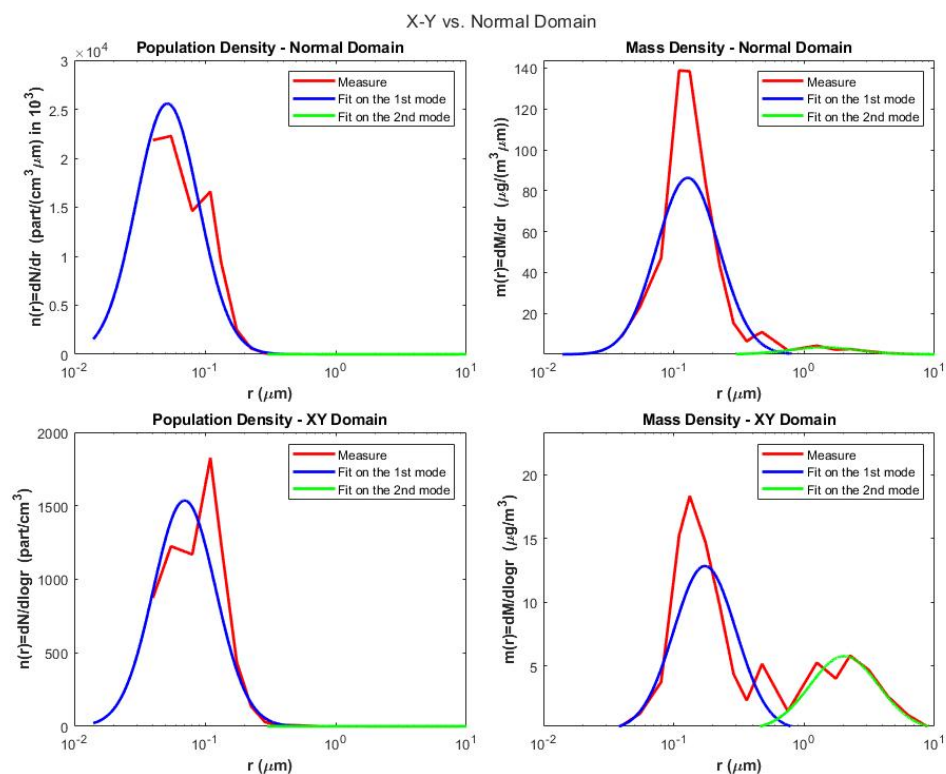


Figure 11: Plots of measure and fit for the first and second modes in both the X-Y domain and the log-normal domain, plotted here in semi-log format.

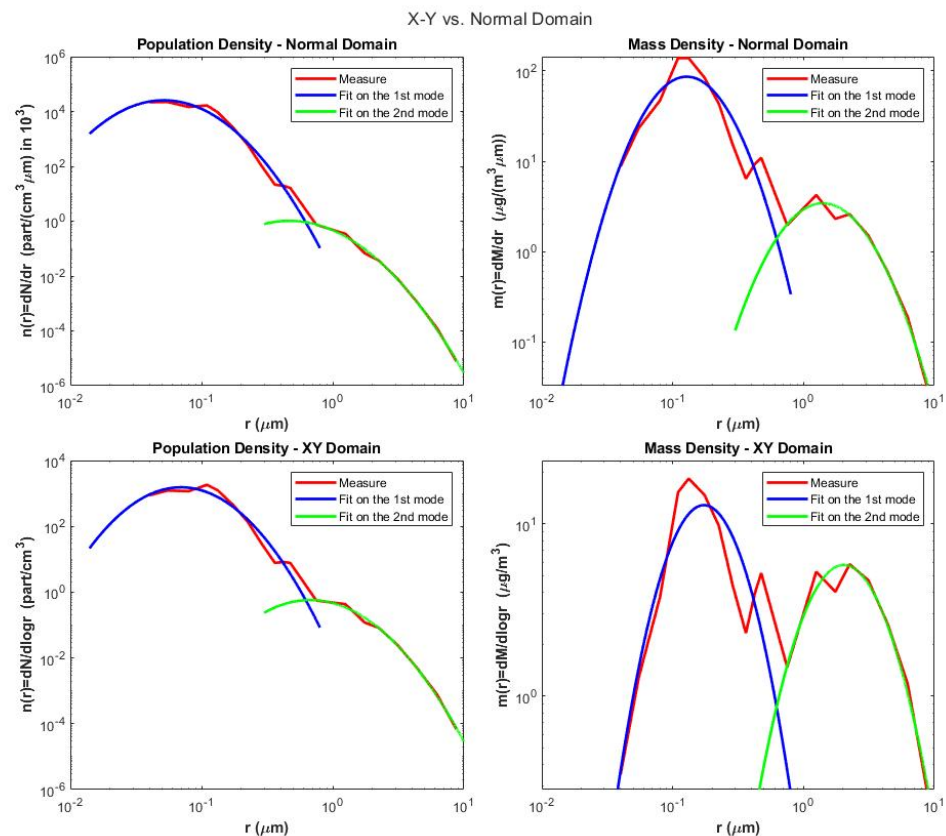


Figure 12: Plots of measure and fit for the first and second modes in both the X-Y domain and the log-normal domain, plotted here in log-log format.

Figures 11 and 12 show the application of the parabolic fit to both the population density and the mass density in X-Y domain and the normal domain. While the difference between the two domains is more evident in the semi-log format of Figure 11, the resulting correlation between the parabolic fit and the measure shown in the table of Figure 9 is more understandable as shown in the log-log format of Figure 12.

4 Conclusions

The production and behavior of aerosols in the atmosphere continues to be a prevalent subject in the atmospheric sciences. The combination of Lidar and laser spectrometers provides a useful tool in the measurement of aerosol species. Moreover, the log-normal theory provides an accurate bases for parameterizing the distribution of both the population density and mass density of measured aerosol species.

References

- [1] Giovanni Pitari, Piero Di Carlo, Eleonora Coppari, Natalia De Luca, Glauco Di Genova, Marco Iarlori, Ermanno Pietropaolo, Vincenzo Rizi, and Paolo Tuccella. Aerosol measurements at l'aquila earlinet station in central italy: Impact of local sources and large scale transport resolved by lidar. *Journal of Atmospheric and Solar-Terrestrial Physics*, 92:116–123, 2013.
- [2] Joyce Penner, Meinrat Andreae, Harold Annegarn, Leonard Barrie, J. Feichter, D. Hegg, Jayaraman Achuthan, R. Leaitch, D. Murphy, and G. Pitari. Aerosols, their direct and indirect effects. *Climate Change 2001: The Scientific Basis. Contribution of Working Group I to the Third Assessment Report of the Intergovernmental Panel on Climate Change*, 289-348 (2001), 01 2001.
- [3] Ina Tegen and Inez Fung. Contribution to the atmospheric mineral aerosol load from land surface modification. , 100(D9):18,707–18,726, September 1995.
- [4] Joseph M. Prospero and Ruby T. Nees. Impact of the North African drought and El Niño on mineral dust in the Barbados trade winds. , 320(6064):735–738, April 1986.
- [5] Cyril Moulin, Claude E. Lambert, François Dulac, and Uri Dayan. Control of atmospheric export of dust from North Africa by the North Atlantic Oscillation. , 387(6634):691–694, June 1997.
- [6] Giovanni Pitari, Glauco Di Genova, Eleonora Coppari, Natalia De Luca, Piero Di Carlo, Marco Iarlori, and Vincenzo Rizi. Desert dust transported over Europe: Lidar observations and model evaluation of the radiative impact. *Journal of Geophysical Research (Atmospheres)*, 120(7):2881–2898, April 2015.
- [7] Colin D. O'Dowd, Michael H. Smith, Ian E. Consterdine, and Jason A. Lowe. Marine aerosol, sea-salt, and the marine sulphur cycle: a short review. *Atmospheric Environment*, 31(1):73–80, January 1997.
- [8] D. M. Murphy, J. R. Anderson, P. K. Quinn, L. M. McInnes, F. J. Brechtel, S. M. Kreidenweis, A. M. Middlebrook, M. Pósfai, D. S. Thomson, and P. R. Buseck. Influence of sea-salt on aerosol radiative properties in the Southern Ocean marine boundary layer. , 392(6671):62–65, March 1998.
- [9] Timothy S. Bates, Vladimir N. Kapustin, Patricia K. Quinn, David S. Covert, Derek J. Coffman, Celine Mari, Philip A. Durkee, Warren J. de Bruyn, and Eric S. Saltzman. Processes controlling the distribution of aerosol particles in the lower marine boundary layer during the First Aerosol Characterization Experiment (ACE 1). , 103(D13):16,369–16,383, January 1998.
- [10] Paulo Artaxo, Eduardo T. Fernandes, José V. Martins, MáRcia A. Yamasoe, Peter V. Hobbs, Willy Maenhaut, Karla M. Longo, and Andrea Castanho. Large-scale aerosol source apportionment in Amazonia. , 103(D24):31,837–31,847, December 1998.
- [11] D. M. Murphy, D. S. Thomson, and M. J. Mahoney. In Situ Measurements of Organics, Meteoritic Material, Mercury, and Other Elements in Aerosols at 5 to 19 Kilometers. *Science*, 282:1664, November 1998.
- [12] Eric E. Gard, Michael J. Kleeman, Deborah S. Gross, Lara S. Hughes, Jonathan O. Allen, Bradley D. Morrical, David P. Fergenson, Tas Dienes, Markus E. Galli, Robert J. Johnson, Glen R. Cass, and Kimberly A. Prather. Direct Observation of Heterogeneous Chemistry in the Atmosphere. *Science*, 279:1184, February 1998.
- [13] Giovanni Pitari, Daniele Visionsi, Eva Mancini, Irene Cionni, Glauco Di Genova, and Ilaria Gandolfi. Sulfate Aerosols from Non-Explosive Volcanoes: Chemical-Radiative Effects in the Troposphere and Lower Stratosphere. *Atmosphere*, 7(7):85, June 2016.

- [14] Hans-F. Graf, Johann Feichter, and Bärbel Langmann. Volcanic sulfur emissions: Estimates of source strength and its contribution to the global sulfate distribution. , 102(D9):10,727–10,738, May 1997.
- [15] Albert Ansmann, Jens Bösenberg, Anatoli Chaikovsky, Adolfo Comerón, Sabine Eckhardt, Ronald Eixmann, Volker Freudenthaler, Paul Ginoux, Leonce Komguem, Holger Linné, Miguel Ángel López Márquez, Volker Matthias, Ina Mattis, Valentin Mitev, Detlef Müller, Svetlana Music, Slobodan Nickovic, Jacques Pelon, Laurent Sauvage, Piotr Sobolewsky, Manoj K. Srivastava, Andreas Stohl, Omar Torres, Geraint Vaughan, Ulla Wandinger, and Matthias Wiegner. Long-range transport of Saharan dust to northern Europe: The 11-16 October 2001 outbreak observed with EARLINET. *Journal of Geophysical Research (Atmospheres)*, 108(D24):4783, December 2003.